Remote Sensing and Modeling of Coherent Structures in River and Estuarine Flows

Andrew T. Jessup
Applied Physics Laboratory
University of Washington
1013 NE 40th St.
Seattle, WA 98105-6698
phone: (206) 685-2609 fax: (206) 543-6785 email: jessup@apl.washington.edu

Robert L. Street
Department of Civil and Environmental Engineering
Stanford University, Stanford, CA 94305-4020
phone: (650) 723-4969 fax: (650) 725-39720 e-mail: street@stanford.edu

Stephen G. Monismith
Department of Civil and Environmental Engineering
Stanford University, Stanford, CA 94305-4020
phone: (650) 723-4764 fax: (650) 725-9720 email: monismith@stanford.edu

Alexander R. Horner-Devine
Department of Civil and Environmental Engineering
University of Washington
Seattle, WA 98195-2700
Phone: (206) 685-3032 fax: (206) 685-9185 email: arhd@u.washington.edu

LONG-TERM GOALS

The long-term goals of this research are to combine state-of-the-art remote sensing and *in situ* measurements with advanced numerical modeling (a) to characterize coherent structures in river and estuarine flows and (b) to determine the extent to which their remotely sensed signatures can be used to initialize and guide predictive models.

OBJECTIVES

Coherent structures are generated by the interaction of the flow with bathymetric and coastline features. These coherent structures produce surface signatures that can be detected and quantified using remote sensing techniques. Furthermore, a number of relationships between coherent structures and flow characteristics have been suggested that have the potential to allow flow parameters (e.g. mean velocity, bottom roughness, shear, and turbidity) to be inferred from remote measurements. The objectives are to test the following four hypotheses:

1. Flow parameters can be inferred from remotely sensed signatures of coherent structures.

2. Numerical models can be constrained with these inferred parameters.

3. The effect of stratification on the strength of coherent structures can be used to detect the presence or absence of stratification and the location of the fresh/salt water interface.

4. Numerical and field experiments can be used together to predict, interpret, characterize, and understand coherent structures.

APPROACH

The key to this project is an interactive process that blends sophisticated remote sensing, in-situ measurements, and numerical simulation. Our approach is to conduct closely coupled field and numerical model experiments to test the hypotheses listed above. The plan includes two major field experiments with both *in situ* and remote sensing measurements – the first occurred in 2006 (Year 2) and the second is planned for 2008 (Year 4). A preliminary experiment was conducted in 2005 (Year 1) to aid in the design of the major field efforts. The research involves four main areas - (1) *in situ* measurements, (2) remote sensing, (3) modeling, and (4) physics and classification of coherent structures. The *in situ* field measurements are used to characterize the overall flow field to investigate the generation of coherent structures at specific sites, and initially, to provide boundary inputs for the numerical models. The surface signatures of coherent structures in the same region are detected using remote sensing techniques and compared with the *in situ* and model results. Results from the *in situ* field observations, remote sensing, and numerical model runs will be synthesized into a classification scheme that includes all observed coherent structures. Predictive scaling relationships will be developed in order to generalize the results from this study to other systems. The result of this integrated approach will be a thorough investigation of the mechanisms and evolution of coherent structures in rivers and estuaries in order to link their surface expressions to subsurface flow features.

The project participants have been organized into teams identified by the main areas of interest listed above: *Remote Sensing*: A. Jessup, C. Chickadel (APL-UW) ,W. Plant (APL-UW), and K. Edwards (APL-UW); *Modeling*: R. Street and O. Fringer (Stanford); *In situ Measurements*: S. Monismith and D. Fong (Stanford); *Physics and Classification:* A. Horner-Devine and P. MacCready (UW-Oceanography).

WORK COMPLETED TO DATE

The focus of this reporting period was analysis of the data from the first major experiment that took place from 3-27 July 2006 and the ongoing numerical modeling effort. This report will highlight progress in the following areas:
- Barge-based Infrared Imaging (UW, APL)
- Airborne Infrared Imaging (UW, APL)
- Estuarine Dynamics (Stanford)
- Physics and Classification of Coherent Structures (UW, Civil and Env. Eng.)
- Numerical Modeling (Stanford)
- Microwave Remote Sensing (UW, APL)

RESULTS

Barge-based Infrared Measurements
Analysis of the infrared imagery collected from the barge platform during the 2006 field deployment was focused on characterizing the spatial and temporal boil signature generated at the submerged sill,

testing a kinematic boil model, and investigating the effectiveness of surface velocity estimates from IR image sequences via a particle image velocimetry (PIV) technique. Previously, we have demonstrated that the thermal signature of boils visible in the IR imagery is the result of vertical temperature stratification. During strong flood and ebb tide flows cold saline water from Puget Sound is transported upwards as boils shed from the submerged sill. These coherent structures erupt at the surface downstream where they are in thermal contrast to the warmer fresh river water at the surface (Figure 1).
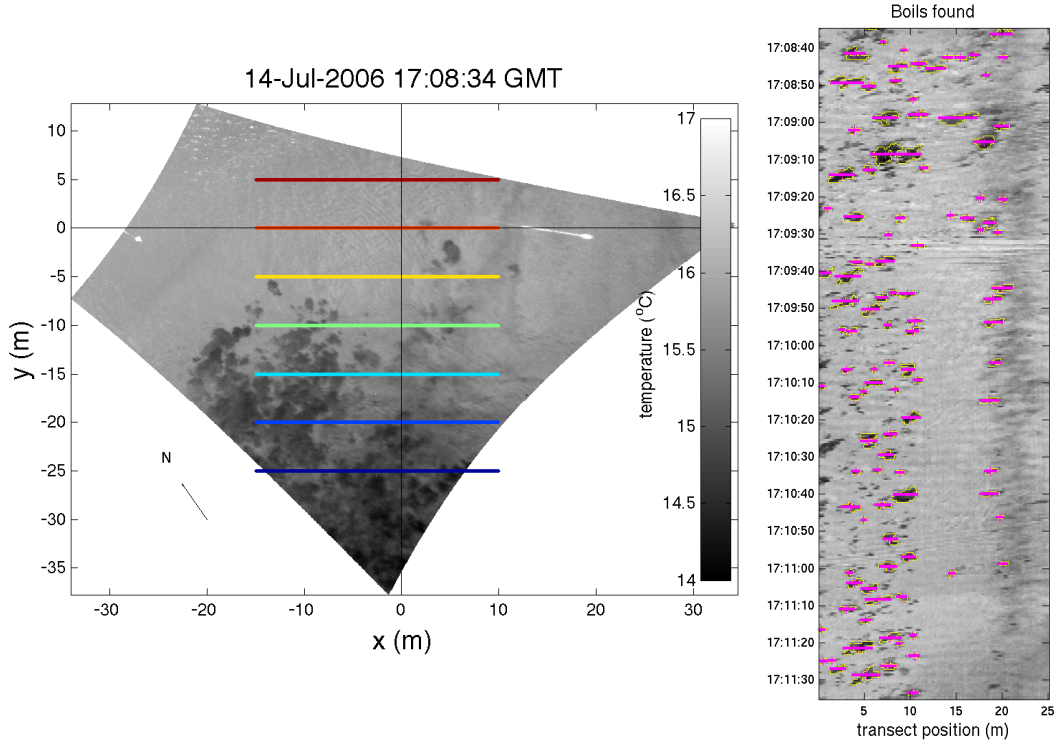

Figure 1. (left) Rectified thermal image of the flow disturbance over the submerged sill. Note the colder (darker) boil eruptions downstream of the sill, which is located at y = 0, parallel with the x-axis. Colored transects indicate arrays for subsequent video analysis. (right) Example time series and automated boil identification from the transect at y = -10m.

To characterize the physical and temporal properties of the boil field, the infrared barge imagery was first rectified to a local coordinate on a frame-by-frame basis using photogrammetric techniques to remove image jitter and motion due to sway of the barge. Registered and rectified images were sampled on discreet pixel arrays parallel to the axis of the sill (Figure 1) to measure and count the boil diameter and frequency with respect to tidal flow. The strong thermal contrast was exploited to segregate the boils via a thresholding technique which revealed an expected spatio-temporal signature where boils erupted increasingly closer to the sill with a decrease in water depth over the sill, as shown in an example in Figure 2. Mean boil sizes appeared to increase in size as the tide ebbed, and were estimated to be approximately 1m at the peak of boil activity (about 1700 GMT).

Spatial and temporal boils statistics were used to evaluate the hypothesis that the observed boils are the result of the surface eruption of upward propagating loops of span-wise vorticity (also called "horseshoe" or "hairpin" vortices). These vortices originate at the submerged sill and are modeled to acquire their vorticity from the vertical shear-layer flow. We tested a vortex dipole model; the simplest

3

two-dimensional approximation to the horseshoe vortices. A brief development of this model is discussed more completely in the section on Physics and Classification of Coherent Structures below. Using this model we compare IR observations of the surface eruption point of the boils, L, with predictions from the vortex pair model,

$$L = \frac{4H^2}{r},$$

which depend only on the representative boil diameter r (taken as the median diameter from IR observations, Figure 2), and the water depth over the sill H (measured *in situ*). Predictions of L due to a free shear layer,

$$L = \frac{H}{0.06},$$

were also tested as a competing hypothesis. It is evident in the example in Figure 3 that the data fit the vortex pair model best, and the free shear layer predicts the surface eruption point to be significantly father downstream than observed. This is consistent with other observations during the experiment.
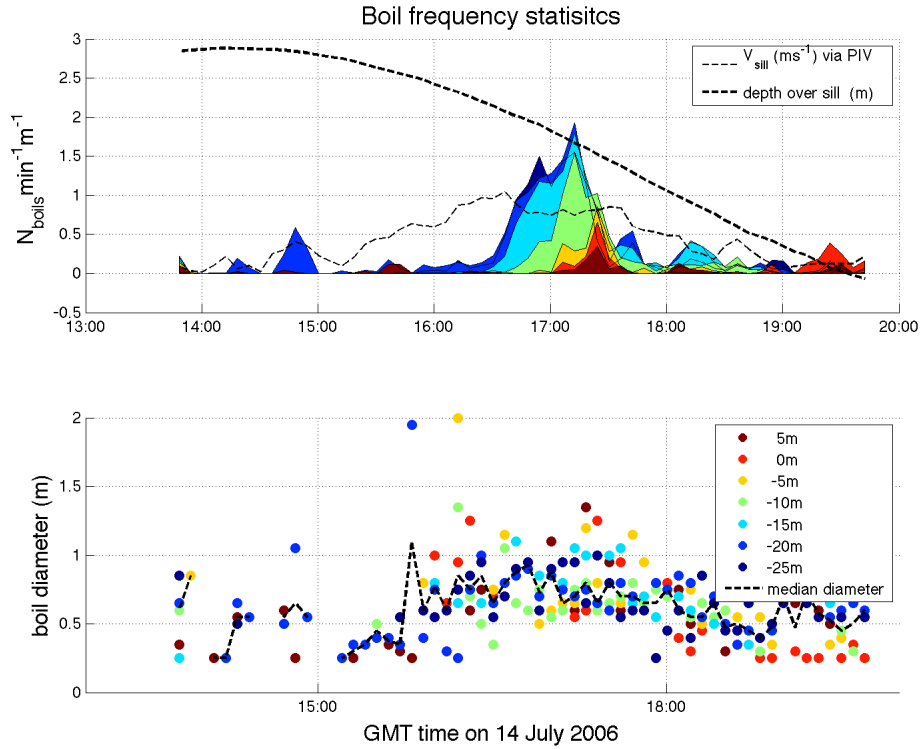

Figure 2. (top) Example of observed boil activity histograms colored to indicate the arrays sampled wrt. the sill, as in Figure 1. (bottom) Estimated mean boil diameter.

Finally, we confirmed it was feasible to estimate surface velocity from surface IR signatures using an existing technique that estimates velocity magnitude and direction in one horizontal dimension using a frequency-wavenumber space method [*Chickadel et al.*, 2003]. Figure 4 shows sample time series of along-stream velocity from the surface PIV technique and a collocated ADCP at a depth of between 0.25 m and 0.50 m. The surface PIV estimates are systematically larger in magnitude than the near surface ADCP measurements, which may be due to the expected vertical velocity shear. Interestingly, at the time when boils are most active on the surface (around 1700 GMT) the surface velocity is nearer

to the velocity of the interior flow. Work continues to understand this difference, as it is likely a direct result of the flow dynamics due to boils. In future work we are extending surface velocity analysis by testing different PIV methods to estimate the two-dimensional flow.
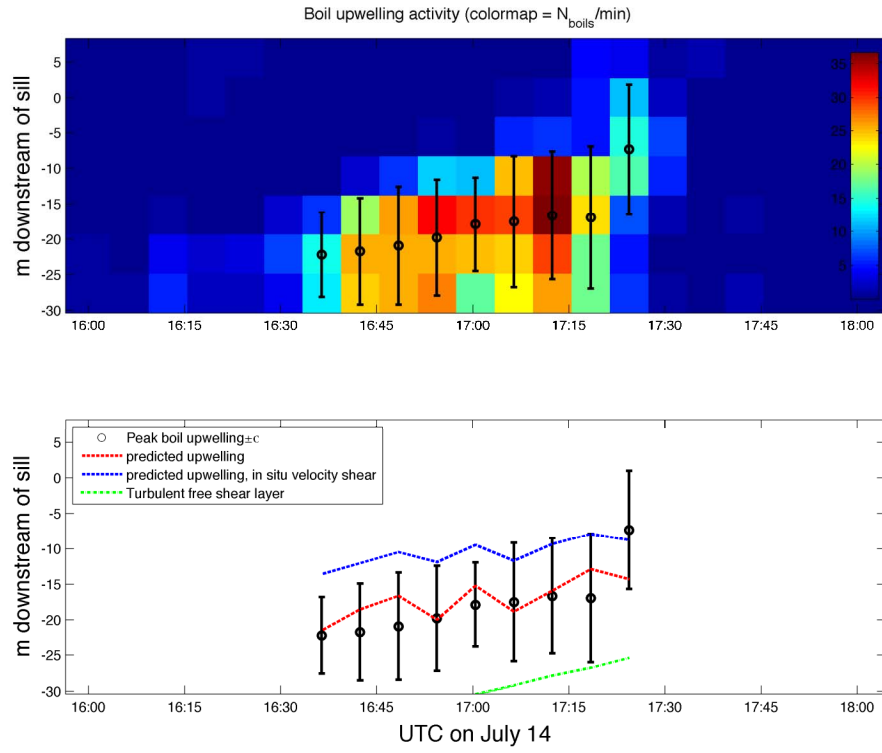

Figure 3. (top) Colormap of relative boil activity observed along the array, and the Gaussian fitted region of peak activity and width (circles with bars, respectively). (bottom) Comparison of the modeled (dashed lines) and observed boil eruption locations.
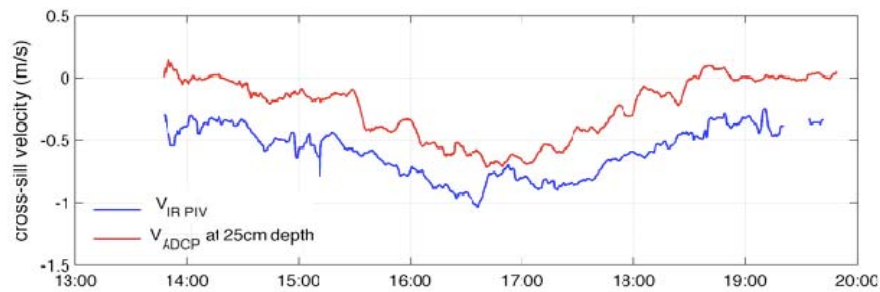

Figure 4. Time series of along-stream PIV surface velocity and near-surface in situ measurements. The consistent offset between the measurements is likely due to strong vertical velocity shear in the region of the sill.

Airborne Infrared Measurements
During COHSTREX 06, a light aircraft collected data with the APL Infrared System, APLIS, as well as a hyperspectral imager, PHILLS, flown by NRL colleagues. The along-river flight track is shown in

Figure 5. On each flight day, 5-20 repeat legs were flown along the track shown in Figure 5, spanning 1-3 hours. The flights were timed to collect data during flood, ebb, and slack tide conditions (Figure 6). Top-to-bottom temperature differences vary with the tide, from well-mixed when river water is present to 1-2 degree stratification when the estuary front is present.

Here, focus is on the APLIS data used to derive maps of the water's skin temperature, T_{skin}. In T_{skin} maps, coherent structures are visible because their vertical motions bring deeper water to the surface, interrupting T_{skin}. The upwelled water is a different temperature due to vertical stratification, the result of the development of a cool or warm skin at the water surface or estuarine inflow. Individual coherent structures of $O(1\ m)$ are captured due the high resolution of the APLIS imagery.
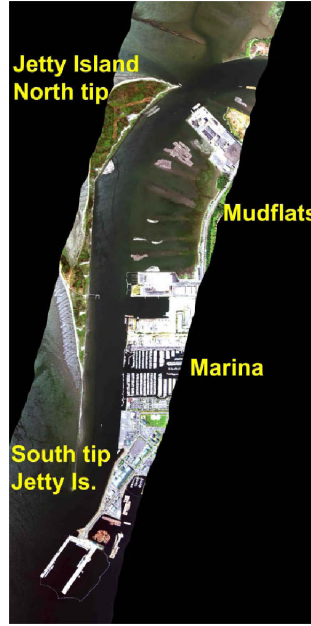

Figure 5: Flight track along the Snohomish River. Both T_{skin} and hyperspectral data were obtained along the track. False-color hyperspectral image shown.
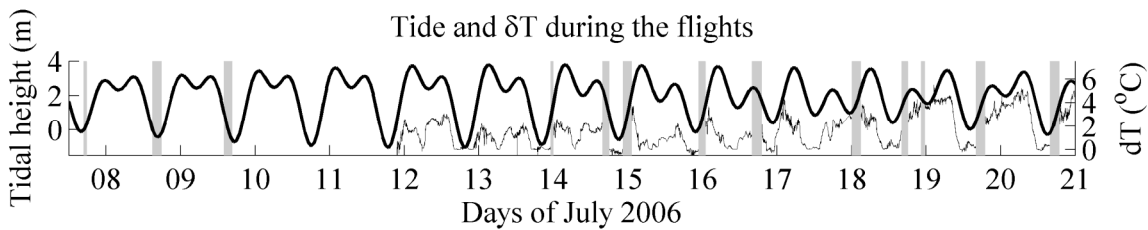

Figure 6: The 13 flights (grey bars). Tidal height (heavy line) and vertical temperature difference, δT (light line), from mooring data near the barge. Flights cover flood, ebb, and slack tide conditions, and stratified and mixed conditions

Coherent structures in aircraft infrared data
Four types of coherent structures are consistently present in the data.

Cold water inside river bend – The flight track (Figure 5) spans a major river bend with a radius of curvature of about 2 km. On the bend's inside wall, cold water appears on all flood tide flights (July 13, 14 PM, 17, 19, and 20) except for weak flood on 18 AM. The cold water is also present on one ebb flight (July 09) but not on other ebb flights (July 14 AM, 16, weak ebb on 18 PM), and not on slack tides. The cold water is 1-2 degrees colder than adjacent waters, similar to the vertical temperature difference observed at the moorings (Figure 6). Its source is hypothesized to be centrifugal upwelling as the river flow rounds the bend, and investigation of this hypothesis is ongoing. An example is shown in Figure 7 from flood tide. Water that is 1 C colder than adjacent water appears inside the bend along the mudflats.

Lateral front off Jetty Island – During flood tide, cold water moves up the river while warmer water inflows from the bypass north of Jetty Island, forming a strong lateral front. This front is seen on all flood tide flights (July 14 PM, 15, 16, 18 AM, and 19) except for a short flight on July 13 and the weak flood during July 18 AM. Boils and lateral instabilities are often observed at frontal interface. An example is shown in the last pane of Figure 7, in which a strong lateral front emanates from the north tip of Jetty Island.
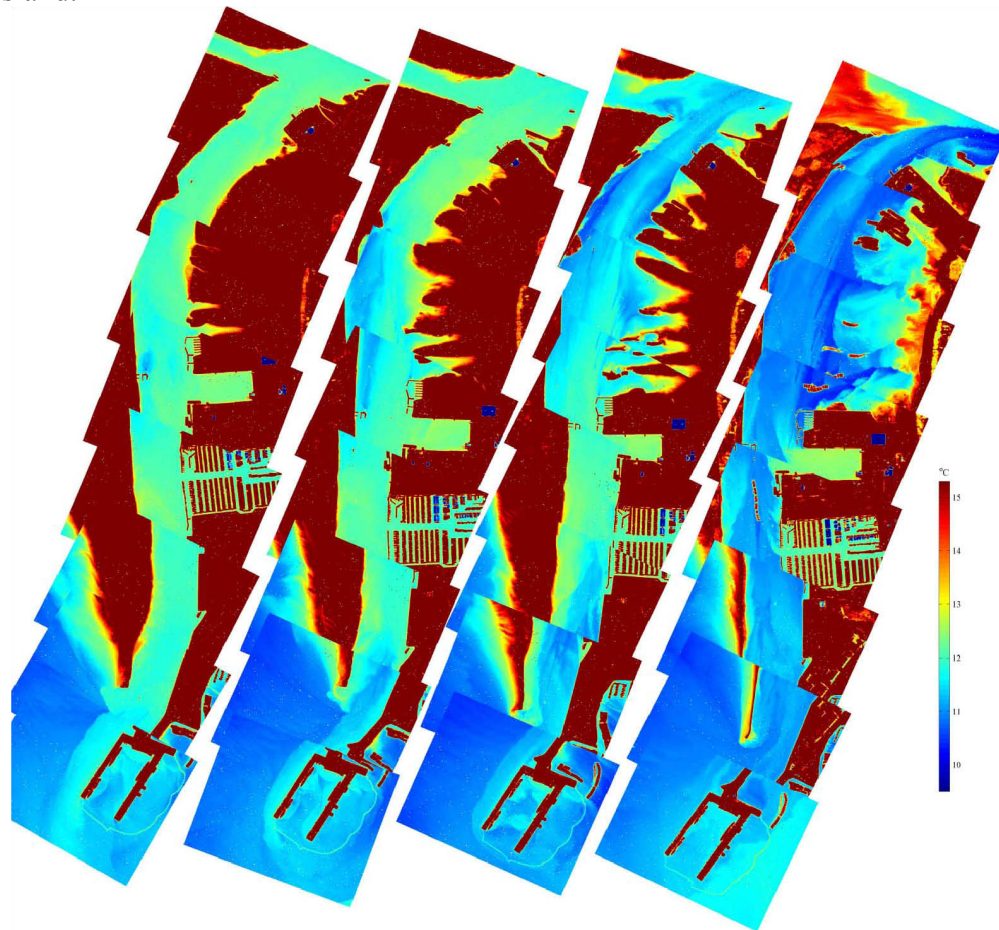

Figure 7: During flood tide on 07/14/2006, long cold wakes first develop from wall irregularities, then cold water appears on the inside of the channel bend (last panel). Between the cold water and a pulse of warm water flowing in from the bypass, a strong lateral front develops.

Boils and gap flow through sill – On the northern tip of Jetty Island, a rocky sill is the site of fast gap flow and turbulent boils. These flow features are seen on most flights, including flood (July 7, 13, 16, 14 PM, 15, 20) and ebb (July 08, 09, 14 AM, 16). On the July 08 flight, cold water streaming through the gap also relatively low in sediment content, based on concurrent hyperspectral imagery. Figure 8 shows an example of the boil-filled cold wake during ebb during the July 14 AM flight. The cold wake extends far downstream (Fig. 8a) and contains vigorous boils (Fig. 8b) which are about 1 degree colder than the background.

Obstacle wakes – Long cold wakes from fixed obstacles such as pilings or irregularities in the channel wall are seen on both flood tide flights (July 14 PM, 15, 18 AM, 19, and 20) and ebb tide flights (July 14 AM and 18 PM). An example is shown in Figure 7, in which a cold wake extends from a manmade structure protruding from the river's western wall. Another example is seen in Figure 8a, in which a long cold wake extends from a sidewall irregularity.
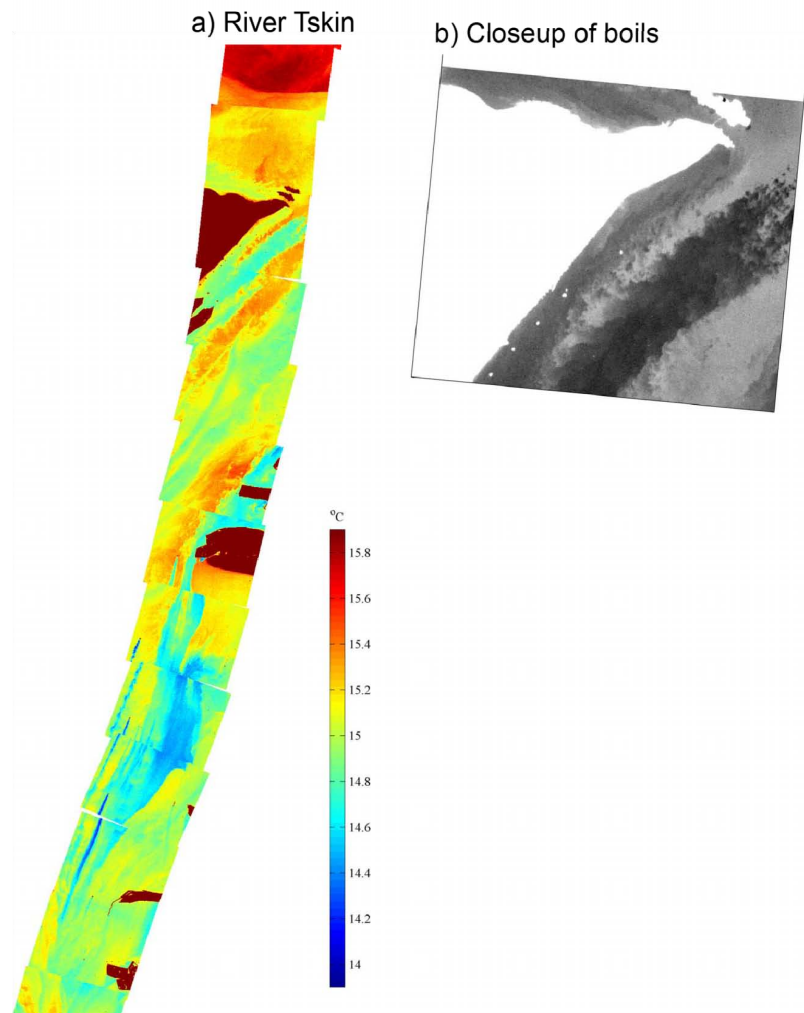

Figure 8: During ebb tide on the July 14 AM flight, a long cold wake extends from Jetty Island's tip (a). Long wakes also extend from sidewall irregularities. (b) Closeup of the cold wake; imagery resolves individual boils. Cold (warm) temperature indicated by dark (light) colors.

Estuarine Dynamics

During the reporting period, our primary focus has been on detailed data analysis of the rich data set provide by the ~95% data recovery of our extensive instrumentation. We have investigated the tidal-averaged estuarine dynamics such as residual circulation, analyzed the salt-wedge propagation and dispersion, as well as focused on detailed frontogenesis mechanisms. Significant emphasis has been placed on work that overlaps with the remote sensing data and modeling efforts, working closely with other team members.

In order to adequately quantify the complex Snohomish hydrodynamics, we deployed six moorings and performed extensive transecting surveys (*Figure*). The four main moorings are centered around the sill on the edges of the channel (M2A, M2B, M3A, and M3B). Each of these moorings resolve along and cross-channel currents and turbulence fields with a bottom mounted fast pinging Acoustic Doppler Current Profiler (ADCP) and Acoustic Doppler Velocimeter. They resolve the density structure with a bottom mounted Conductivity Depth Temperature (CTD) sensor and two CTDs mounted to a floating buoy/pole system. Finally, moorings M4 and M6 both resolve velocity with upward looking Doppler profilers and mooring M4 recorded density with a bottom mounted CTD.

In addition to the moored deployments, two thirty-hour intensive surveys were completed during representative spring and neap tides. These surveys included ADCP transects in a square path around the sill and along-channel CTD transects. We completed five successful REMUS missions and one twelve-hour cross-channel CTD survey between moorings M3A and M3B.
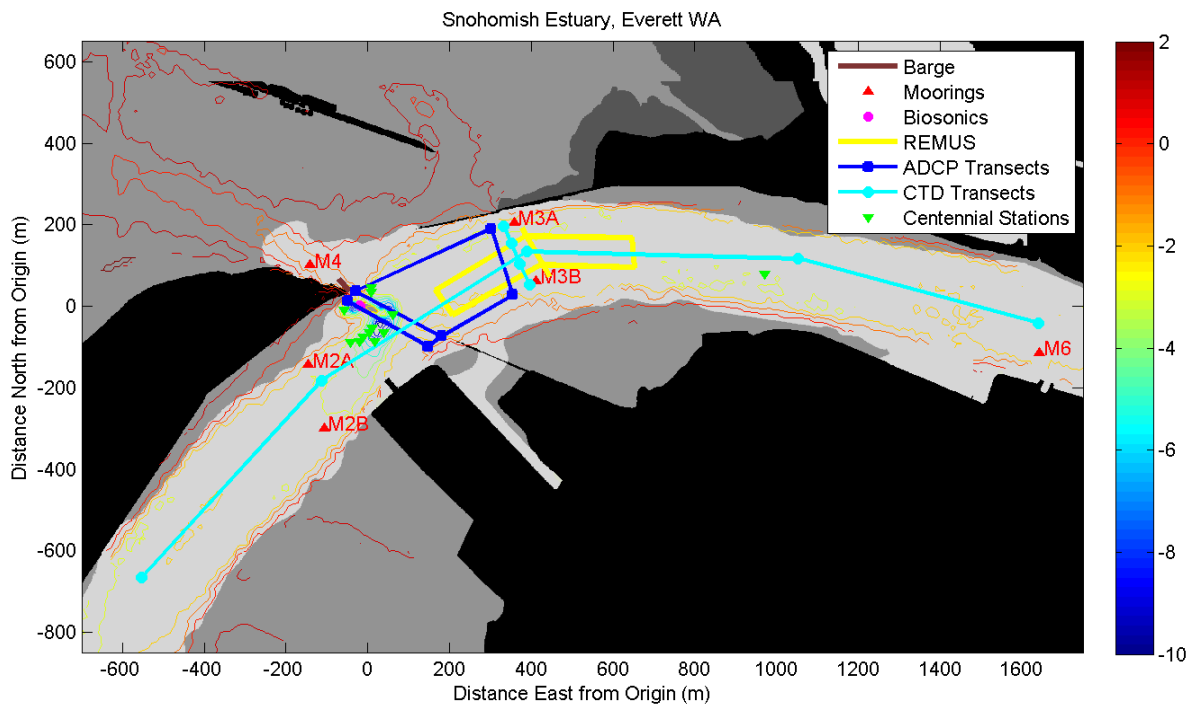

Figure 9. July 2006 Experiment Mooring and transect locations are marked on a map of the Snohomish River Estuary. Dark grey represents intertidal regions and bathymetry is marked in meters below MLLW.

The velocity, depth, and density data help characterize the Snohomish River Estuary system. The system is a salt-wedge estuary with top to bottom density differences ranging from zero to 20 kg m^{-3}. Maximum currents in the system exceed 1.5 m s^{-1}. Water level is dominated by the M_2 semidiurnal and K_1 diurnal tidal constituents and the tidal wave is close to standing with a slightly progressive nature. The tidal range exceeds 4 m, while the depth is only 2.5 m below MLLW classifying the Snohomish as a shallow, macrotidal system.

Examining tidally averaged parameters in this system highlights the need for better interpretation of these quantities in a shallow, macrotidal system. The depth averaged residual circulation exhibits a counterclockwise circulation around Jetty Island; this has important implications for transport in the system (*Figure* 10 left). The depth dependent residual circulation exhibits a complicated vertical structure due to the competition of traditional estuarine gravitational circulation (upstream at depth and downstream at the surface) with residual circulation driven by tidal non-linearities (downstream at the bed) (*Figure* 10 right). This competition as well as residual circulation driven by bathymetric complexity is important in macrotidal, salt-wedge systems. We are continuing to examine the implications for interpreting these tidally averaged quantities by investigating salt transport and the importance of Stokes drift in the Snohomish. This data has been used to help validate the numerical model, and we will continue to interact with the modeling team, expecting that the model can help us better interpret these quantities.
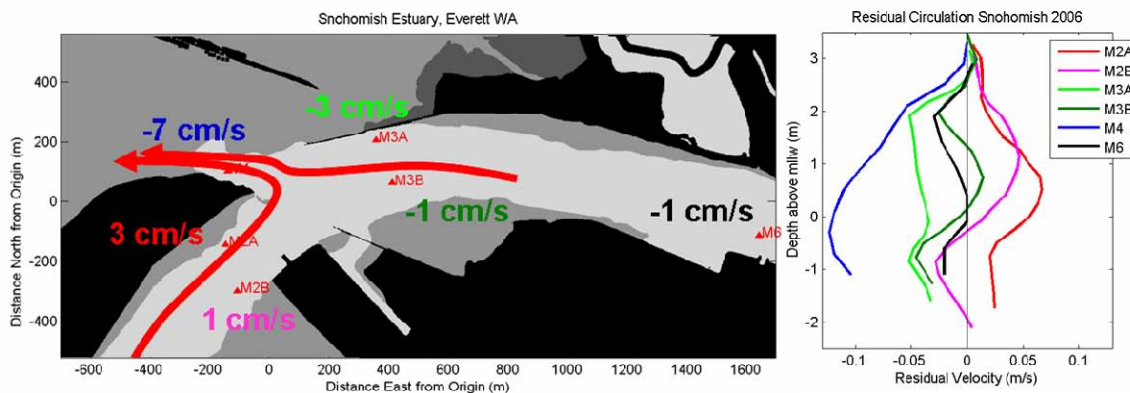

Figure 10. Snohomish Residual Circulation computed from the moored velocity profilers (depth averaged on left, depth dependent on right). Positive velocity is upstream (flooding current) and depths are meters above MLLW.

In addition to assisting the modelers, we have been working closely with the remote sensing team to understand both the salt-wedge propagation and frontal features observed remotely. Both visual and infrared remote sensing data identify the salinity intrusion front. The salinity intrusion front is V shaped indicating a strongly plunging inflow. The propagation of the salt-wedge (the subsurface head of the salinity intrusion) is well documented by both our moored instrumentation and along channel CTD transects. The salt-wedge propagation matches theory well and exhibits expected neap/spring variability (*Figure*).

The in-situ measurements have corroborated that remote sensing can determine when the system is stratified based on the temperature of boils. This has suggested that we may be able to back out other

salt-wedge parameters such as propagation speed by examining spatial and temporal changes in boils and/or wakes from submerged objects or boats.

The remote sensing data and in-situ data provide additional corroboration in understanding other frontal features. The complex bathymetry of the Snohomish creates a trapping mechanism that leads to frontogenesis. The front consistently forms off of the tip of Jetty Island during flood tides after lower low water. The in-situ data, ADCP transects, CTD transects, as well as REMUS have identified the frontogenesis mechanism and its interaction with transverse circulations, vertical mixing, and stratification. Remote sensing data verifies the frontal presence.
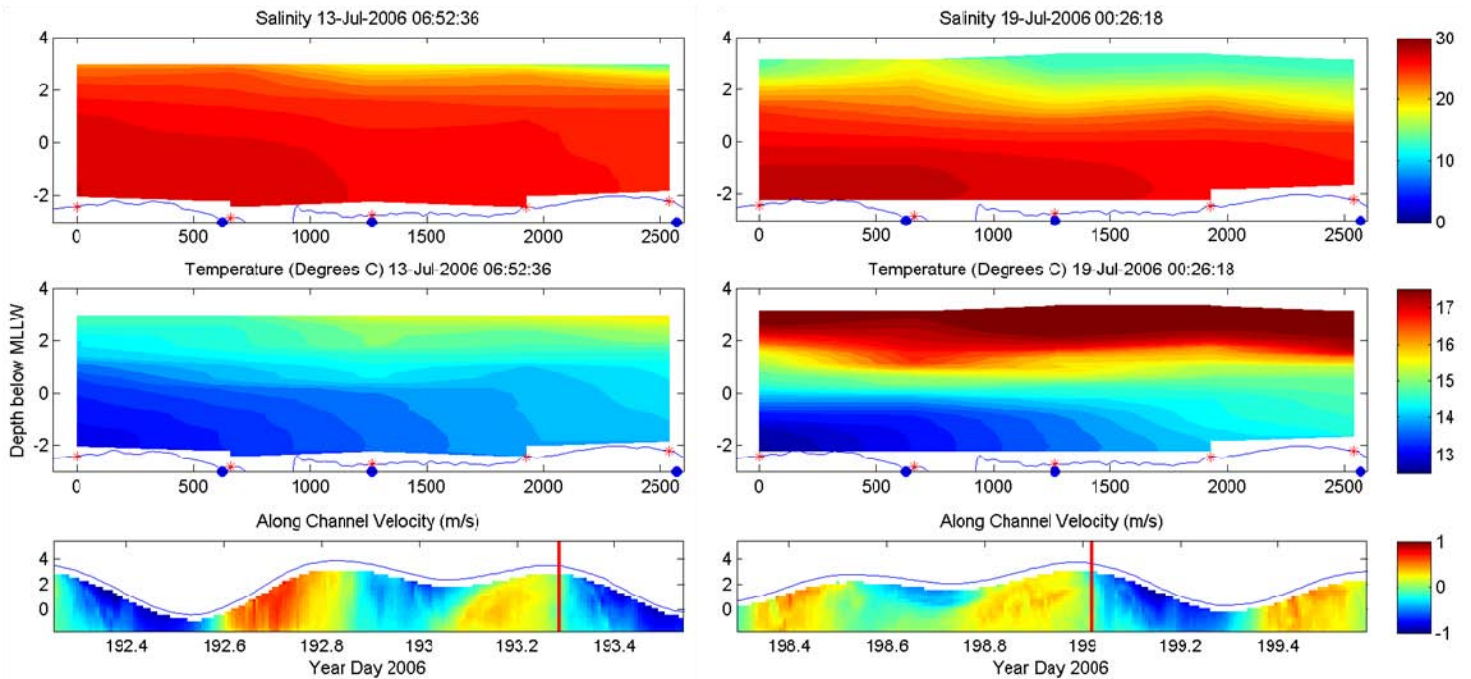

Figure 11. Salt-wedge maximum observed intrusion distance. Plots include (top down) salinity, temperature, and velocity. Left panels are from the spring survey, right panels are from the neap survey. Salinity and temperature are along channel snapshots from a CTD transect. The velocity is over the entire 30 hour survey throughout the water column as measured by the M3A ADCP. The CTD transect snapshot time is marked with a red line.

Moored instrumentation, CTD transects, and REMUS observe mid-density water trapped in the mudflat bypass towards the end of ebb. During mid-flood, the mid-density water is pushed onto the outer bank of the main channel. This leads to transverse baroclinic forcing which drives a secondary circulation cell in the opposite direction to that forced by channel curvature (*Figure*). The competition between transverse baroclinic forcing and centrifugal accelerations creates two transverse circulation cells which are convergent at the surface. This convergence manifests itself in a sharp front visible at the water surface and in the infrared imagery due to the different temperature of the water masses on either side of the front. Lateral baroclinic forcing and the reduction of centrifugal acceleration allow the front to propagate across the channel.

11

This front affects vertical mixing and stratification across the channel. While the front is located between the two moorings (i.e., mid-channel), stratification stabilizes the water column on the outer bank where (mooring M3A) mixing only occurs near the bed, while at the inner bank (mooring M3B) mixing occurs throughout the water column. By the time the front propagates across the full channel width, stratification is enhanced across the channel and mixing is suppressed.
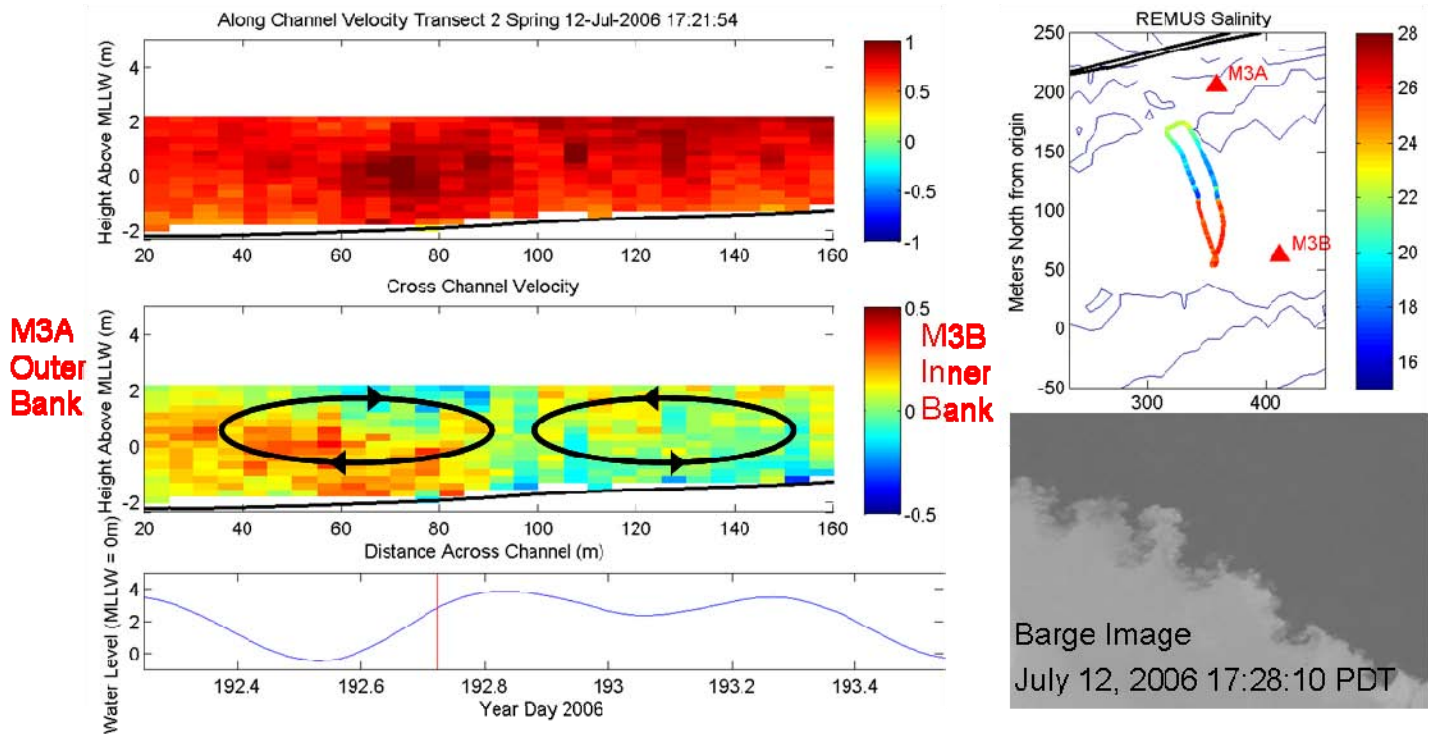

Figure 12. Transverse Circulations and Density form a surface convergence mid-flood. ADCP transect data on the left show along and across-channel velocity. The infrared barge image taken 7 minutes after the ADCP transect corroborates the frontal presence. Salinity from REMUS provides detailed cross channel density distributions on a different day during the same part of the tidal cycle.
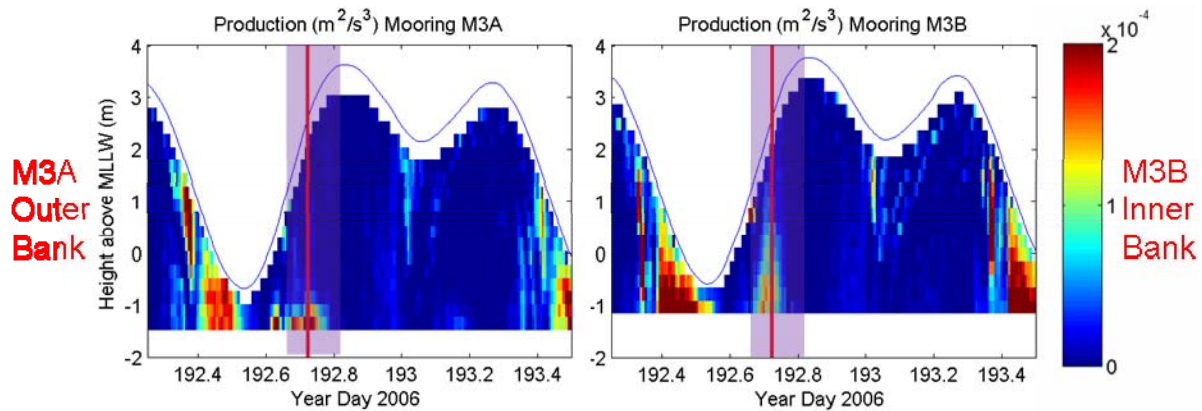
Figure 13. Vertical Mixing is represented by turbulent kinetic energy production computed with the ADCPs. The red line marks the time of the Figure transect and the band represents the time period when the front is present.

In summary, the in-situ data has provided us with insight into the fundamental hydrodynamics of the Snohomish River Estuary. The data is being used to calibrate the numerical model and investigate features observed in the remote sensing data. The observed frontogenesis mechanism is a striking example demonstrating the powerful overlap of the in-situ data, UUV measured data (REMUS), and remote sensing in understanding the system dynamics.

Physics and Classification of Coherent Structures
In situ measurements made during the 2006 field experiment focused on the physics and classification of coherent structures include velocity (ADCP) and acoustic backscatter (Biosonics) from instruments mounted in an upward-looking configuration on the estuary bottom immediately downstream of the sill and within the infrared (IR) field of view. This configuration enabled direct comparison between the data acquired with the bottom-mounted instruments and the remote sensing data and, thus, extension of the surface information through the water column. In addition to the moored instruments, CTD casts were made in the region immediately downstream of the sill during the ebb on July 21 in order to observe the evolution of the vertical density structure leading up to and during the period of boil generation.

Analysis of the velocity, backscatter and density data has focused on answering three questions:
1. What critical conditions (velocity, stratification, height of water over sill) lead to the generation of boils?
2. What is the subsurface structure (depth, width, slope) and frequency of the boils observed in the lee of the rocky sill on ebb tide?
3. Do the observed boils consist of discreet packets of fluid that are carried to the water surface from the generation site, or are they simply the largest eddies within the spectrum of eddies generated in the shear layer formed by the flow over the sill?

CRITICAL CONDITIONS

Figures 14 a-c show the acoustic backscatter, sill-normal velocity and salinity during the ebb tide on July 21. In the acoustic backscatter the water surface shows up as a region of high return (yellow) that descends over the course of the tide. Below the surface the gross structure of the water column is clear.

Early in the ebb, horizontal layers of higher return indicate vertical stratification and there is little acoustic return from water in the lower water column, consistent with clear (cold and salty) water from Puget Sound. As the ebb progresses, higher-frequency vertical structures are observed. The onset of boils occurred shortly after 11:00 based on careful examination of the Biosonics data. This is marked by a vertical black line in Figure 14 a-c. The onset time of boils was determined for each day of the study and compared well (r^2=0.66) with an independent determination of boil onset time based on the IR data. Near-surface velocity and velocity shear increase sharply in the period leading up to boil generation (Figure 14b and f). Vertical stratification, which is high at the level of the sill before boil onset, decreases at the time of boil generation. As shown in Figure 14f, the acceleration of the surface layer due to the ebbing tide and the decrease in stratification combine to drive the densimetric Froude number, Fr, above 1. On July 21, boil onset occurred when Fr=1. By extending the stratification data to other days based on mooring upstream and downstream of the sill, we have also determined the critical condition for other days in the study. These results indicate that boil onset is observed in the Biosonics data once the Fr is significantly higher than 1 during the spring tide. This is attributed to larger water depth over the sill at boil onset, which causes the boils to surface further downstream and makes them harder to image with the Biosonics. The boil propagation model described shortly is being used to correct for this sampling bias.
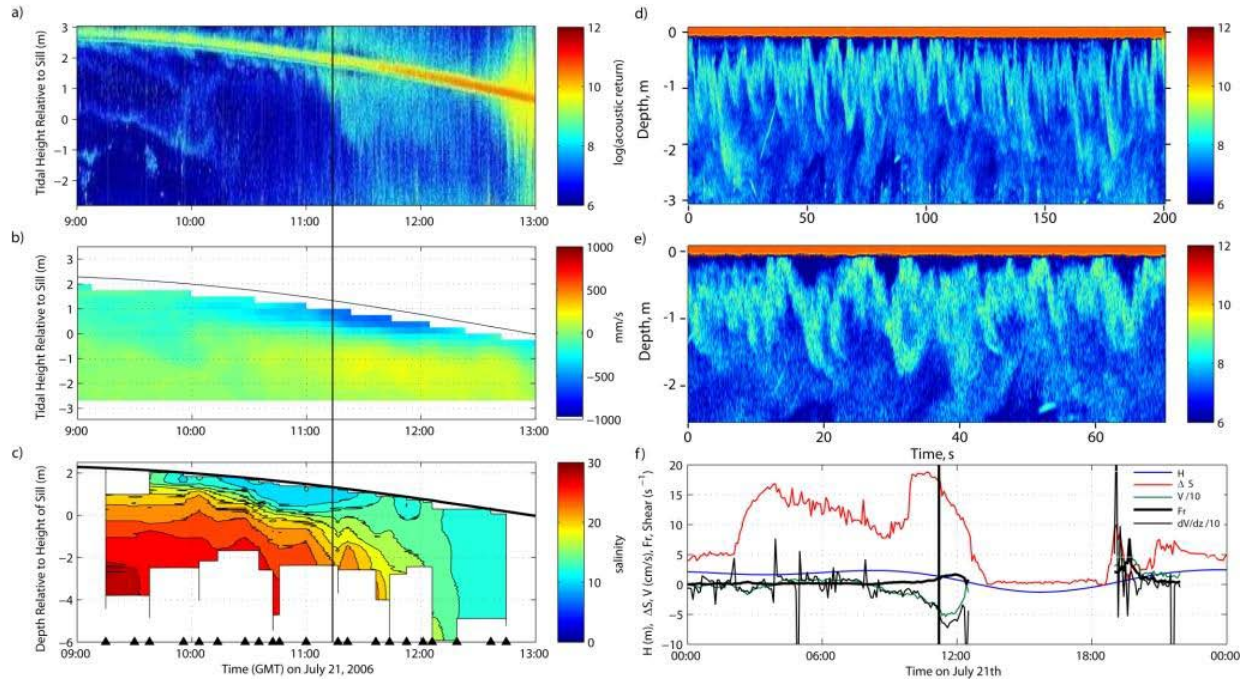

Figure 14: a) Acoustic return from the upward-looking Biosonics echosounder during the ebb tide on July 21, 2006. b) Velocity structure and c) salinity in the region immediately downstream of the sill during the July 21 ebb. Note that the velocity is positive upstream and perpendicular to the sill. The vertical black line indicates the boil onset time. d) 200 s zoom and e) 70 s zoom of the boils as they appear in the acoustic backscatter. f) Surface height relative to the sill (blue), top-to-bottom salinity difference (red), surface layer velocity divided by 10 (green), velocity shear divided by 10 (thin black) and densimetric Froude number (thick black) on July 21st. The black vertical line indicates the boil onset time.

14

Subsurface structure

Boils appear in the backscatter data as regions of low acoustic return near the water surface that are bounded from below by a band of high acoustic return fluid (Figure 14d and e). The high acoustic return is the result of suspended particulate from the river, turbulent microstructure or, possibly entrained bubbles. The near-surface band of high return is much more pronounced around the time of boil onset, suggesting that the boils may contribute to this signal, either due to elevated turbulence levels or entrained bubbles. In the core of the boils a pocket of low return fluid is typically observed. Comparison with the timing of cold boils observed at the water surface in the IR data suggests that the low return may be an indicative of cold, salty Puget Sound water that is being ejected from the lower layer. Based on a combination of manual and spectral analysis of the Biosonics data, the depth is observed to scale approximately with the height of water over the sill and the boil width is approximately 0.8 m. The average frequency observed for all boils in the study is 0.06 hz and no consistent spring/neap variation was observed. Finally, a lagged correlation between two vertically spaced time series of acoustic return in the near-surface boil region was used to determine the onset slope of the boils. This slope was then adjusted to account for velocity shear in the water column. Using this technique, the boils were observed to have an onset slope of approximately 45 degrees. The variation of slope under different conditions has not been evaluated yet.

Vertical boil propagation

In order to test the hypothesis that boils are discreet packets of fluid that are ejected from the shear layer a simple model for their vertical propagation speed was developed. The model assumes that the boil is generated in the region of high shear immediately downstream of the sill. The boil detaches from the sill and kinks, forming a hairpin vortex similar to those observed in the boundary layer (Figure 15). In our model, the vertical propagation speed is based on the propagation speed of a vortex dipole. The dipole inherits the vorticity of the shear layer (U/H) and is characterized by a cross-sectional area equal to the observed boil size. Based on these assumptions, the propagation speed of the boil is estimated as $w_b = \dfrac{Ur}{4H}$, where r is the boil size. This estimate of the vertical speed can also be used to predict the location that boils will surface downstream of the sill for a given water depth $L = \dfrac{4H^2}{r}$. This prediction was tested favorably in the Barge-based infrared measurements section above (see Figure 3).
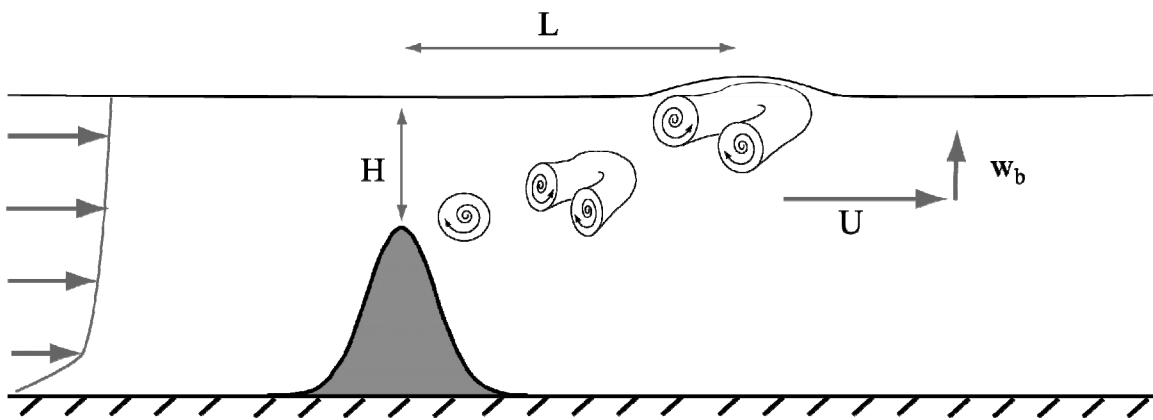

Figure 15: Cartoon of the boil generation mechanism and vertical propagation.

15

The observations and quantification of boil parameters based on the 2006 field experiment was the subject of Bronwyn Hayworth's MS thesis. She has now graduated and is employed locally. We have hired a postdoc, Dr. Stefan Talke, who will continue with the analysis of the 2006 data and aid with preparation and execution of the planned 2008 experiment.

Numerical Modeling

During the past year we have focused on refining our simulations by employing improved bathymetry and higher grid resolution and adjusting the bottom drag coefficients, the boundary conditions, and the turbulence model in order to achieve simulation results that match field data extremely well.

Grid and bathymetry

Figure 16 depicts the grid we are currently using. This grid has roughly 2 million grid cells with a resolution of 8 m near the study site and 300 m in Puget Sound. The vertical resolution ranges from 0.25 m in the upper 5 m of the water column to 30 m in the deeper reaches of the Sound. High-resolution bathymetry surveys conducted by the COHSTREX field team enabled us to employ accurate bathymetry in the vicinity of the study site, which is crucial to correctly simulating the velocity field in the area. Figure 17 depicts this bathymetry. Although the simulations employ high resolution, it is still not high enough to capture the features of the prominent sill at the study site. Therefore, in order to simulate the disturbance in the bulk flow resulting from the exposure of the sill crest at low tide, the elevations of 4 cells were raised by 0.5~1 m above MLLW. The locations of these cells were determined from the infrared imagery. Hydrostatic simulations with this grid and bathymetry employ a time step size of 1 s and are roughly twice as fast as real time using 32 processors on the ARL Major Shared Resource Center computers.

Comparison to observations

Free-surface

Simulations were performed during the period 12 July 2006 (year day 192) to 23 July 2006 (year day 205), which encompasses roughly one spring-neap cycle. Predictions of free-surface height are compared to the observations at three locations in Figure 18, namely at a location in the sound (Figure 18a), at USGS Gage Station 12255500 which is upstream in the Snohomish River (Figure 18b), and Mooring M3b located in the channel near the study site (Figure 18a). The predictions show good agreement with the observations, although at mooring M3b, the amplitude of strong ebbs is slightly underpredicted (<0.3 m) and the phase of strong ebbs is lagged (<30 min), with the maximal deviation occurring at spring tide. Furthermore, the predicted strong ebbs are less symmetric. This is likely due to the ELM scheme which is used for advection of momentum, which results in significant dissipation when linear interpolation is used (Wang, 2005; McCalpin 1988; Staniforth and Cote 1991). Also as a result of numerical diffusion, excessive low momentum fluid from channel shoals is diffused into deeper portions of channels (Zhao et al., 2006). These effects are most severe at LLW when channels become shallow and shoals become dry. Despite these drawbacks, ELM is still the best choice for momentum advection because of its favorable stability properties.
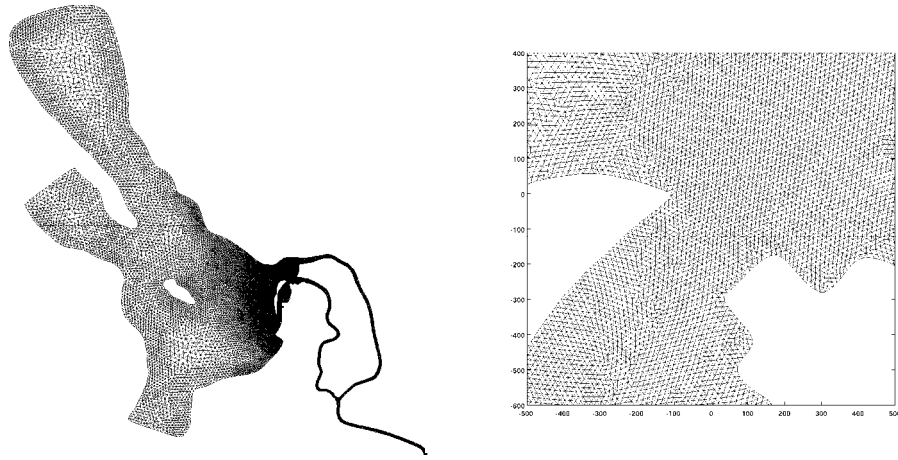
Figure 16: Unstructured grid of the simulation domain (left) and a zoomed-in view of the high-resolution grid in the vicinity of the study site (right).
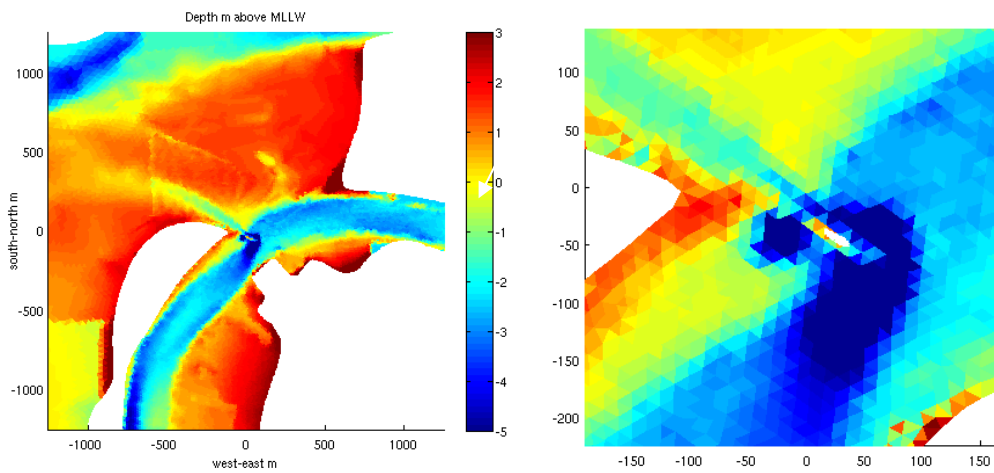

Figure 17: High-resolution bathymetry (in m) interpolated onto the SUNTANS grid in the vicinity of the study site. The right panel depicts a zoomed-in view of the study site with the four exposed cells that represent the sill crest in white.
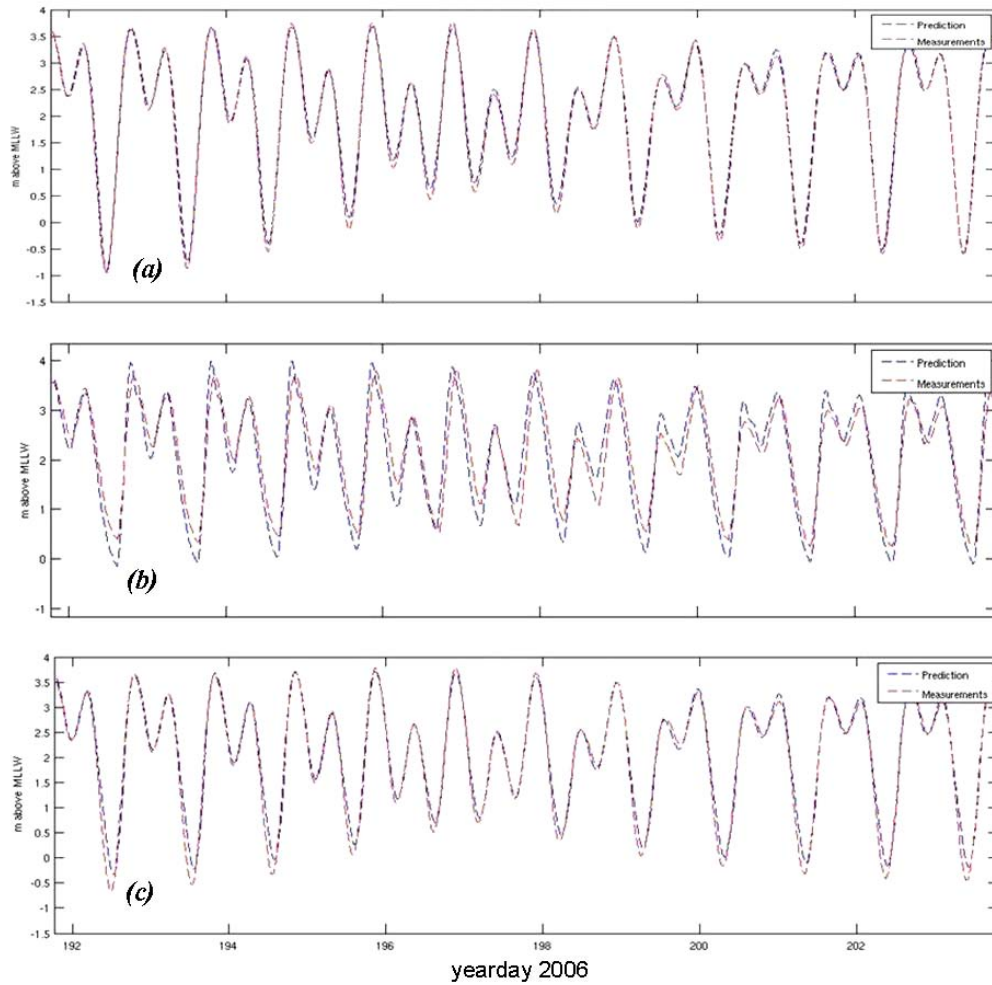
Figure 18: Comparisons of free surface height (a) in the sound, (b) at the gage station and (c) at M3b. Predictions: blue dashed line, Observations: red solid line.

Currents

Figure 19 compares the predicted 10min- and depth-averaged along-channel velocities to the observations at two mooring locations near the study site (see Figure 9 for these mooring locations). Figure 19(a) represents results at mooring M3b which is the same mooring location for Figure 18(c), while Figure 19(b) represents results at mooring M4 which is located in the bypass. Positive velocities indicate upstream in the direction of the flood tide.

At mooring M3b, both phase and magnitude of velocity are predicted well. At mooring M4, the predictions match the observations reasonably well, but we attribute the differences between the predictions and observations to the complex bathymetry in the region which makes the simulations highly sensitive to grid resolution and, more importantly, to the resolution of the bathymetry. The presence of the shallow mudflats in the bypass region leads to a shut off of the bypass during large ebbs which adds additional variability to the flow. Early in the ebb, water flows freely into the sound via the bypass. However, when the free surface drops sufficiently low (roughly 1 m above MLLW), the bypass shuts off when more and more of the mudflat is exposed. As the tide continues to ebb, the fluid trapped in the bypass reverses and flows back into the river, which leads to a tidal reversal during

18

late stages of the ebb tide in the bypass. This flow reversal is evident in the higher-frequency nature of the currents at M4, which display a frequency that is roughly twice as high as that at M3b. While SUNTANS captures this flow reversal, the currents on the flood tides tend to be over predicted (the green dashed peaks in Figure 19b). These results are likely due to the lack of high-resolution bathymetry data for most of the tidal flats to the north of the study area, including Steamboat Slough. Deeper waters in these regions can lead to weaker friction during flood tides which causes stronger flood currents through the bypass.
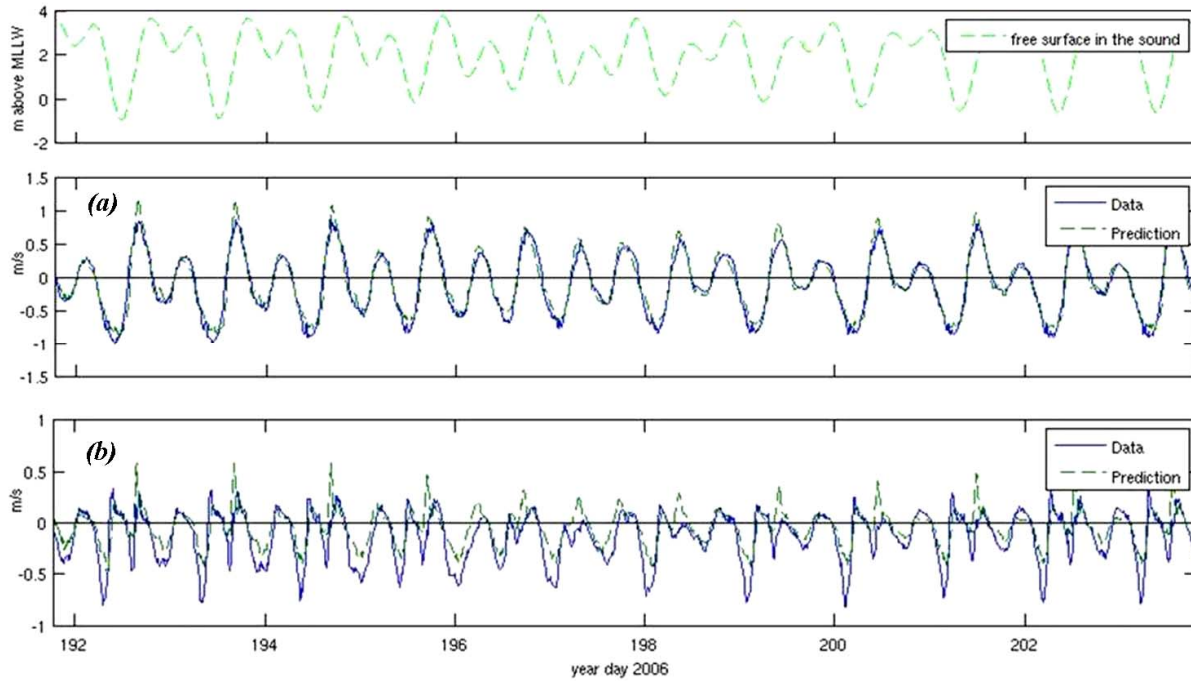

Figure 19: 10min- and depth-averaged along-channel velocities at (a) mooring M3b and (b) mooring M4. Predictions: green dashed line, Observations: solid blue line. See Figure 20 for mooring locations. The top panel depicts the free-surface height in the Sound for reference.

Salinity
Figure 20 depicts the evolution of top/bottom salinity at the moorings over one tidal cycle, and shows how the predictions match the observations well. In particular, the predictions match the observations most closely during the strong flood, when the salinity front arrives and is well-mixed in the vertical. This match indicates that the predicted horizontal salinity gradient matches the observed value of roughly 5 psu/km. During the weak ebb, vertical stratification develops and persists through half of the cycle. As we expected, the model overpredicts the duration of this stratification (it starts earlier and ends later) because, as described by Stacey et al (1999), the Mellor-Yamada 2.5 turbulence closure scheme does not respond quickly enough to the transition between weak and strongly stratified states. We plan on testing other turbulence closure schemes in order to improve this prediction.
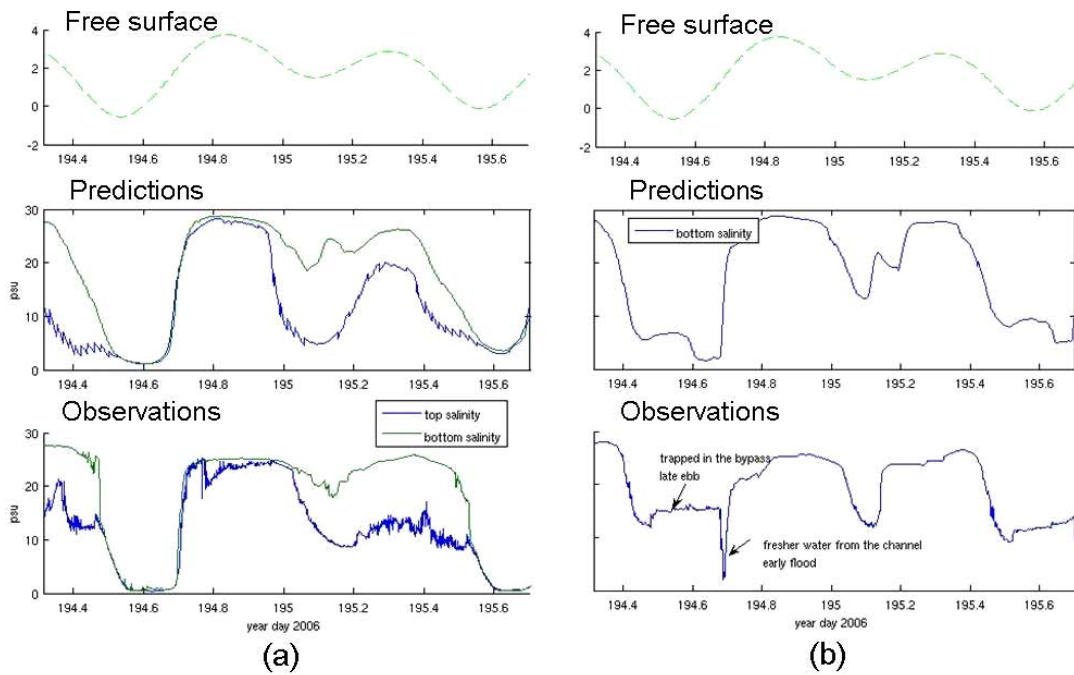
Figure 20: Comparison of predicted vs. observed salinities at mooring M3b (a) and M4 (b). The top row presents the free surface in the Sound for reference, while the middle row displays predicted salinities (top = blue, bottom=green), and the last row displays observed salinities. Note that no top salinity data was available for mooring M4.

Figure 21 illustrates the surface salinity field at the study site during different stages of a strong tidal cycle (note the extensive regions of exposed mudflats during low water), and shows how the complex bathymetry in the region has a significant effect on salt transport. As is observed in the aerial IR images (except warm water is a surrogate for the fresh water we refer to here), a front forms between the bypass water and the more saline river water where they meet during late flood. This occurs because of a lag in the salt transport over the mudflats and through the bypass relative to the main river channel. As the balance between the sides evolves with the rising water level, the front slowly rotates from a longitudinal configuration (Figure 21 lower left) to be more transverse (Figure 21 lower right), which is consistent with REMUS measurements and IR images.
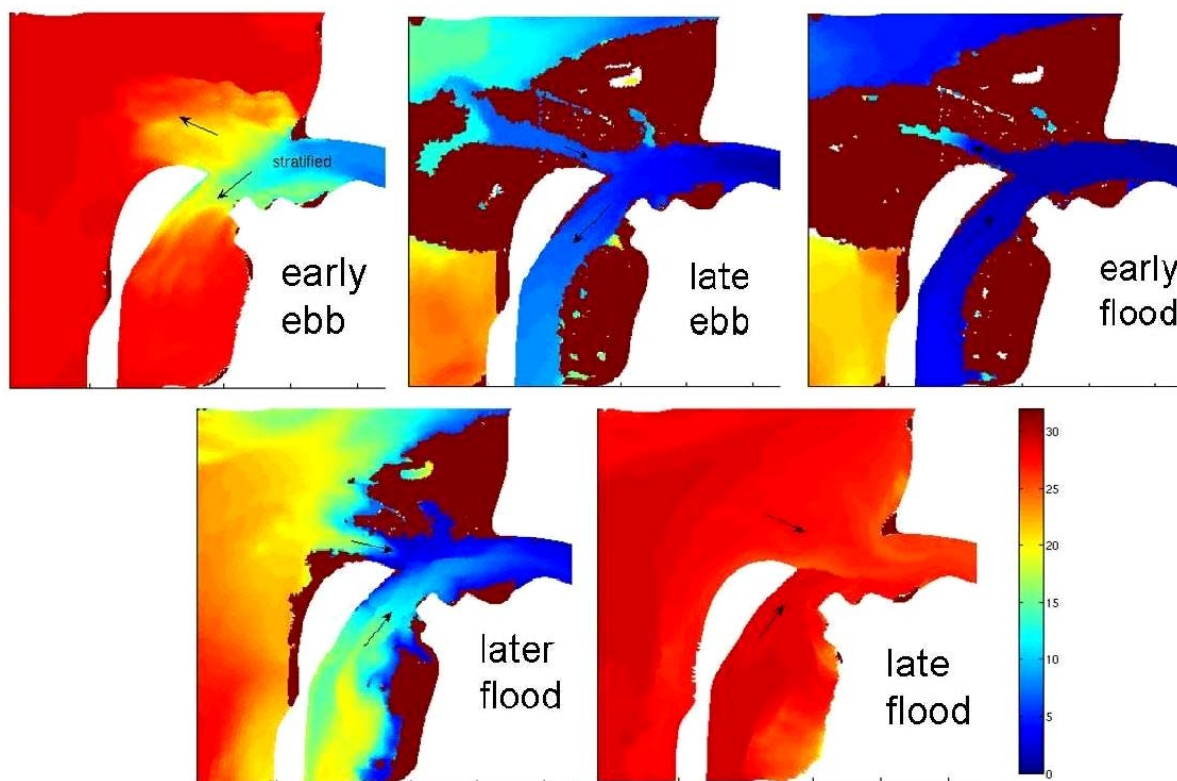
Figure 21: Surface salinity field (in psu) around the study site at different stages of the tidal cycle. Dark red regions represent exposed tidal flats at low water.

Microwave Remote Sensing

In the main experiment in 2006, the microwave amplifier in the airborne CORAR radar failed, the HH polarized Riverscat unit on the barge exhibited very large levels of noise, and a large fraction of the data from the bankside RiverRad radar was lost. Much of the year in 2007 was spent trying to compensate for these failures.

We obtained a DURIP grant from ONR and are in the process of building a new CORAR and upgrading the old one. The end result will be two nearly identical CORAR units that will enable us to operate on both aircraft and ships. The software for these radars is written and testing will begin as soon as the hardware is ready. Final construction of the hardware is awaiting the microwave amplifiers, which have been ordered.

We have analyzed the Riverscat data collected simultaneously with the IR imagery on the aerial lift of the barge. The measurements were made just downstream of the sill. Figure 22 shows time series of various quantities obtained from these measurements.

The scatterer velocities fluctuate around zero because the antenna was directed across the mean flow most of the time. Cross sections are highest near low tide when the sill was exposed. Interestingly, the highest cross sections, corresponding to the roughest surface occurred at low tide when flow over the sill is only due to river outflow. The intensity of the peak of the Doppler spectrum is another measure of this roughness and obviously confirms the cross section results. In both cases the maximum intensities tended to occur at the lowest low tides. Finally, the RMS scatterer velocities obtained from

21

the widths of the Doppler spectrum indicate that the RMS value of the turbulent velocity fluctuations averaged about 0.25 m s^{-1} at low tides but were above this value for high high tides and below it for low high tides.
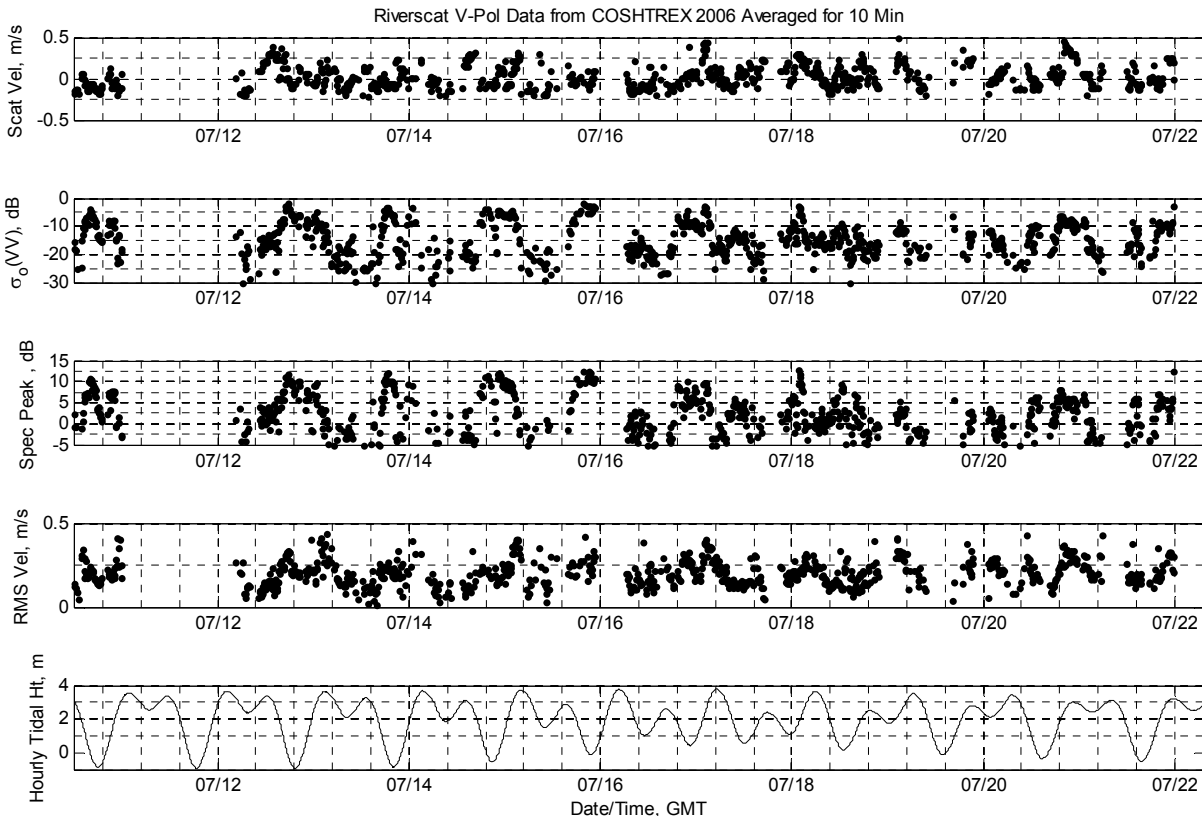

Figure 22. Time series of quantities measured by the vertically polarized Riverscat unit during COHSTREX 2006. The bottom panel shows the tidal height.

We redeployed RiverRad across from the sill from August 2 to September 13, 2007. Comparison of the results of these measurements with those of two years earlier showed that most of the observed features remained constant over that time. Figure 23 shows an example of this for the front that is observed around the tip of Jetty Island on flood tide.

A somewhat more intriguing feature that was observed in the microwave return in both 2005 and 2007 was a stationary double-track feature. This feature is shown in the cross section images in Figure 24; it is also observed in images of scatterer velocity as a feature with zero velocity. Note that it appears near low tide in both images of Figure 24.

The fact that the signature of this feature appeared in exactly the same location in images taken two years apart made us suspect that it might be the surface signature of something on the bottom.   To check this, we attempted to relate the location of this feature to a sidescan sonar image of the region that had been taken as part of COHSTREX. Figure 25 shows the result of this collocation. Although the result is suggestive, we cannot definitely associate the double tracks with the ridge that is oriented similarly.
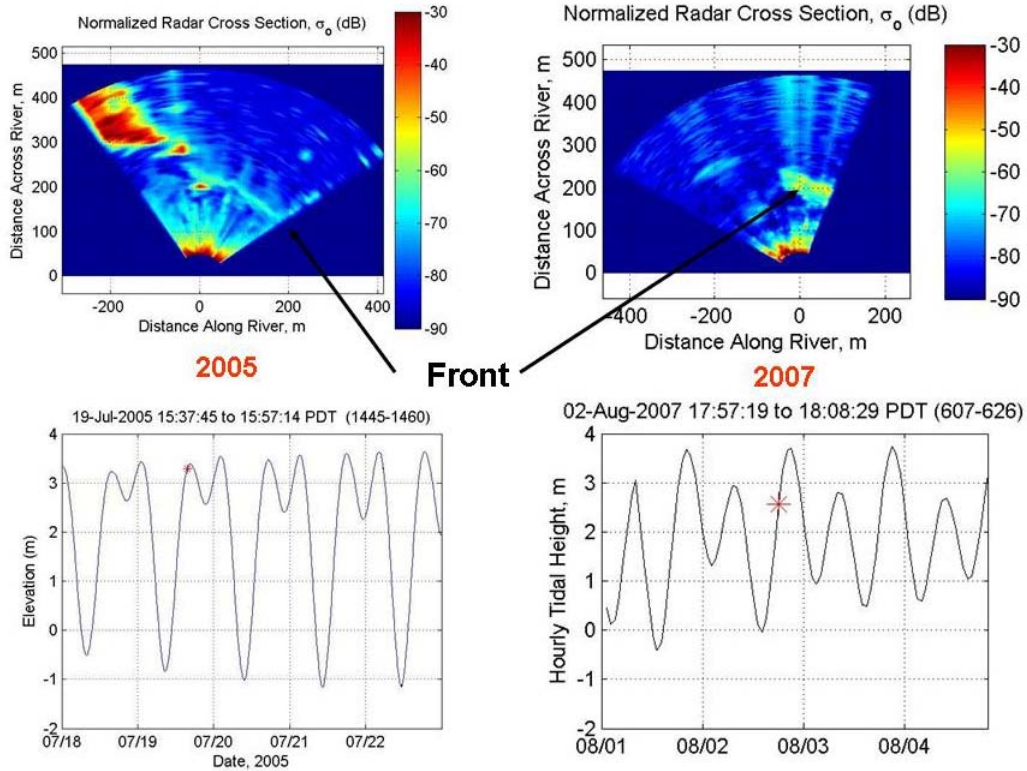
Figure 23. Surface signature of front between returning overflow water and water in the main stream of the Snohomish River observed in both 2005 and 2007 at similar tidal phases.
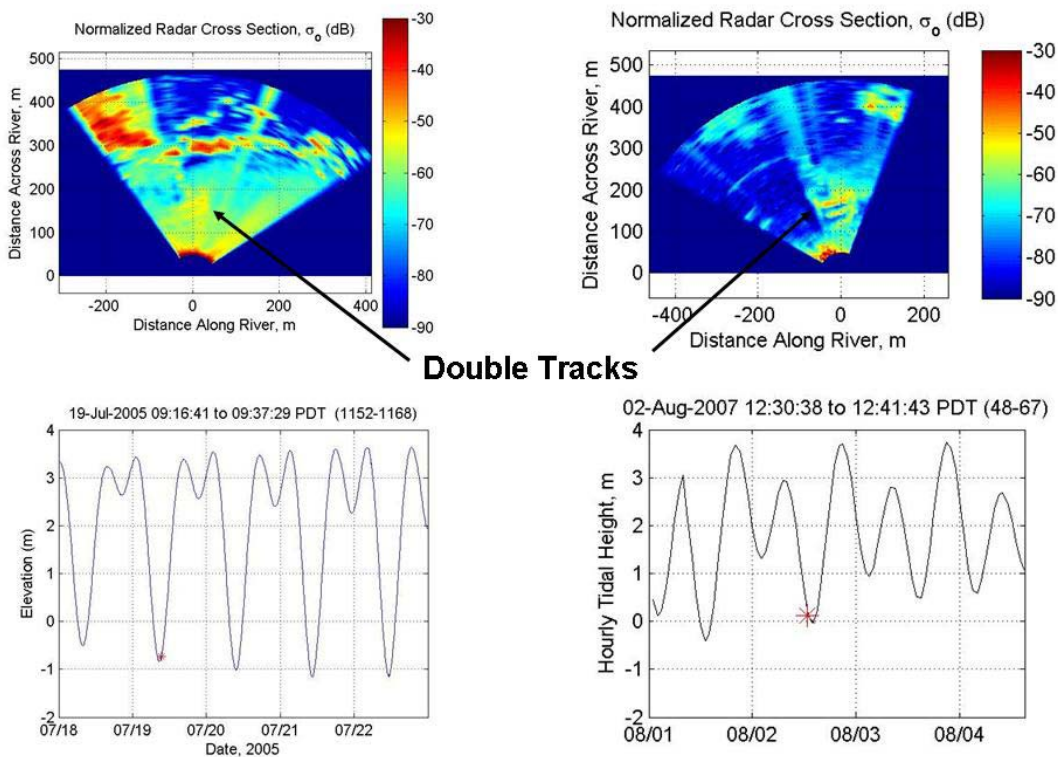

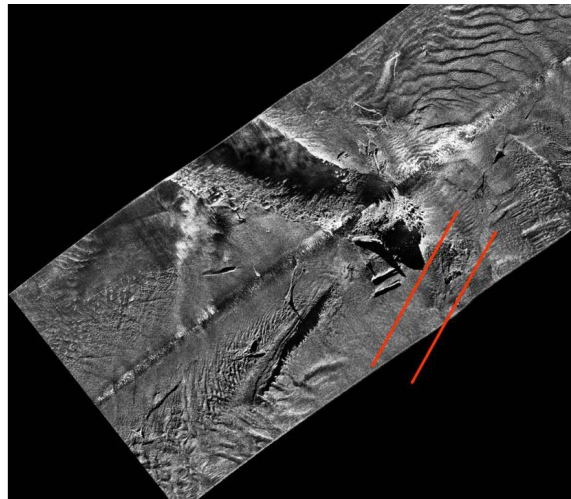***Figure 24. Feature observed in both years 2005 and 2007 at the same location.***

***Figure 25. Location of microwave surface signature of double tracks (red) on a
sidescan sonar image showing a similarly oriented ridge. The distance between the red
tracks is approximately 20 m.***

IMPACT/APPLICATIONS

Our results demonstrate how currently available prediction schemes and observing systems (remote
sensing and AUVs) can be combined for operational applications.

RELATED PROJECTS

None to date.

REFERENCES

Chickadel, C.C., R.A. Holman, and M.F. Freilich (2003), An optical technique for the measurement of
    longshore currents, *Journal of Geophysical Research*, *108* (C11), 3364.

McCalpin J.D., 1988. A quantitative analysis of the dissipation inherent in Semi-Lagrangian advection.
    Monthly Weather Review, 116, 2330-2336.

Stacey M.T., Monismith S.G., Burau J.R., 1999. Observations of turbulence in a partially stratified
    estuary. Journal of Physical Oceanography, 29, 1950-1970.

Staniforth A., Cote J., 1991. Semi-Lagrangian interpolation schemes for atmospheric models- A
    review. Monthly Weather Review, 119, 2206-2223.

Wang J. 2005. Nonhydrostatic numerical modeling of littoral internal waves on an unstructured grid.
    PhD Dissertation, Department of Civil and Environmental Engineering, Stanford University, 166pp.

Zhao, G., 2006. Application of the complementary volume method to simulation of flows on an
    unstructured grid, Proceedings of the Sixteenth International Offshore and Polar Engineering

Conference, San Francisco, California, USA. The International Society of Offshore and Polar Engineers. 402-405.

PUBLICATIONS

B. Wang and O. B. Fringer, 2007, "Modeling the dynamics of the Snohomish River Estuary with a finite volume, unstructured-grid parallel coastal ocean simulator", Proceedings of the fifthinternational symposium on environmental hydraulics, to appear.

B. Wang, O. B. Fringer, and R. L. Street, 2006, "Application of an unstructured-grid, finite-volume parallel coastal ocean simulator to the Snohomish River Estuary", Proceedings of the fifth international workshop on unstructured mesh numerical modeling of coastal, shelf and ocean flows.